Deep-Red-Emitting Colloidal Quantum Well Light-Emitting Diodes Enabled through a Complex Design of Core/Crown/Double Shell Heterostructure

Farzan Shabani, Hamed Dehghanpour Baruj, Iklim Yurdakul, Savas Delikanli, Negar Gheshlaghi, Furkan Isik, Baiquan Liu, Yemliha Altintas, Betül Canımkurbey, and Hilmi Volkan Demir*

Extending the emission peak wavelength of quasi-2D colloidal quantum wells has been an important quest to fully exploit the potential of these materials, which has not been possible due to the complications arising from the partial dissolution and recrystallization during growth to date. Here, the synthetic pathway of (CdSe/CdS)@(1-4 CdS/CdZnS) (core/crown)@(colloidal atomic layer deposition shell/hot injection shell) hetero-nanoplatelets (NPLs) using multiple techniques, which together enable highly efficient emission beyond 700 nm in the deep-red region, is proposed and demonstrated. Given the challenges of using conventional hot injection procedure, a method that allows to obtain sufficiently thick and passivated NPLs as the seeds is developed. Consequently, through the final hot injection shell coating, thick NPLs with superior optical properties including a high photoluminescence quantum yield of 88% are achieved. These NPLs emitting at 701 nm exhibit a full-width-at-half-maximum of 26 nm, enabled by the successfully maintained quasi-2D shape and minimum defects of the resulting heterostructure. The deep-red light-emitting diode (LED) device fabricated with these NPLs has shown to yield a high external quantum efficiency of 6.8% at 701 nm, which is on par with other types of LEDs in this spectral range.

1. Introduction

Semiconductor colloidal quantum wells (CQWs), also known as nanoplatelets (NPLs), make an exciting group of nanocrystals with tight 1D exciton confinement, demonstrating highly promising properties by their possible design of heterostructures.[1–3] The size- and shape-dependent properties of these materials alongside with various electronic structures enable them for a vast range of optoelectronic applications[4] including light-emitting diodes (LEDs),[5,6] luminescent solar concentrator,[7] photodetectors,[8] lasers,[9–11] and photocatalysts.[12] These NPLs offer such advantages over their spherical counterparts, colloidal quantum dots (CQDs), as they possess giant oscillator strengths,[13,14] larger absorption cross-sections,[15–17] and enhanced molar extinction coefficients.[18] While inhomogeneous broadening is a major drawback of CQDs, NPLs with constant ensemble thickness, exhibit much narrower emission bandwidth.[19,20]

CdSe NPLs are among the most studied CQWs, offering a suitable platform as a base material to further design and synthesize complex heterostructures. In its zinc blend crystalline structure, increasing the thickness along [001] direction, normal to the basal planes,[21] can be performed mainly through one of the two strategies: i) One/two-pot synthesis of thick NPLs[22,23]

F. Shabani, H. Dehghanpour Baruj, I. Yurdakul, S. Delikanli,
N. Gheshlaghi, F. Isik, Y. Altintas, B. Canımkurbey, H. V. Demir
Department of Electrical and Electronics Engineering
Department of Physics
UNAM – Institute of Materials Science and Nanotechnology
Bilkent University
Ankara 06800, Turkey
E-mail: hvdemir@ntu.edu.sg, volkan@bilkent.edu.tr
S. Delikanli, H. V. Demir
Luminous! Center of Excellence for Semiconductor Lighting and Displays
School of Electrical and Electronic Engineering
Nanyang Technological University
50 Nanyang Avenue, Singapore 639798, Singapore

B. Liu
School of Electronics and Information Technology
Sun Yat-sen University
Guangzhou 510275, China

Y. Altintas
Department of Materials Science and Nanotechnology
Abdullah Gül University
Kayseri TR-38080, Turkey

B. Canımkurbey
Central Research Laboratory
Amasya University
Amasya 05100, Turkey

and ii) deposition of a shell with a different composition. While direct synthesis of CdSe NPLs with 2–7 monolayers (MLs) have so far been reported in the literature, increasing the thickness above 7 MLs with maintained purity is only possible through colloidal atomic layer deposition (c-ALD).[22–26] Deposition of each layer decreases the electron and hole confinement, and is a possible way to tune the emission peak between discrete energy levels.[27] However, the final material obtained from c-ALD usually suffers from low photoluminescence quantum yield (PLQY) and in some cases the emission even dies out.[25,28,29] Covering the lateral sides of CdSe NPLs with a higher bandgap material, a heterostructure, which is known as core/crown, can increase the PLQY of bare CdSe core up to around 90% without changing the emission peak position.[27,30] On the other hand, the second material can be grown in the thickness direction which, unlike the core/crown, gives rise to extended leakage of electron's wavefunction into the shell.[31] Recently, hot injection (HI) method has been proposed and developed for the NPLs, which yields much higher QYs with ease of synthesis.[32,33] HI is a powerful technique that enables the synthesis of high-quality NPLs with a spectral coverage from 550 to 650 nm, which may be obtained conventionally through shell thickness or alloying the core, shell or both.[34,35]

In contrast to all of the aforementioned strategies to tune the emission peak of the CdSe-based NPLs, it is yet a major challenge to further extend the emission coverage to longer wavelengths, while keeping the 2D shape of the NPLs intact. Having the bulk bandgap energy of CdSe to be around 1.712 eV, theoretically it is possible to exceed the emission peak of 700 nm.[36] There are several reports of CdSe/CdS core/shell in the literature for giant quantum dots, in which the emission peak can be pushed up to around 640 nm.[37–39] For the 4 ML CdSe core NPLs, the thick shell of CdS, corresponding to 14 MLs, gives an emission peak of 670 nm with moderate QY of 50–60%.[32] However, when the shell is alloyed with zinc, the PLQY can boost up to unity at the expense of emitting below 655 nm.[40–42] Herein, it is of primary importance to extend the emission peak of these high-quality NPLs to longer wavelengths without compromising their properties. This is especially important as the emitters in this region have poor PLQY and large full-width-at-half-maximum (FWHM),[43] or are chemically unstable,[44] which diminishes their performance in optoelectronic applications. In the recent years, colloidal NPLs have shown excellent performance with superior properties for laser and LED applications, which is originated in their visible range tunability, photostability, and high PLQY.[34,35,45] Developing high-performance CdSe-based NPLs can compensate the lack of good emitters for electroluminescence (EL) applications at longer wavelengths by employing their excellent properties as active material in LEDs. The deep-red to near infrared light is important for applications of telecommunications and light vision devices.[46,47] Moreover, because of the weak light absorption and scattering from biological tissues at longer wavelengths, this light is particularly useful for biosensing and biomedical applications.[48]

In this work, we propose and show a meticulous synthesis pathway toward the best optimized heterostructure to address the pivotal requirements of a CdSe-based emitter with the lowest possible energy. The seeds for the final HI are designed to be laterally large and passivated, and enable a relatively large

vertical thickness, so that through the final HI shell coating the thickness can be effectively increased. This strategy yields very thick NPLs, emitting closer to the theoretical bulk bandgap energy of CdSe. These thick NPLs were implemented in LEDs as active material, emitting above 700 nm with excellent external quantum efficiency (EQE) of 6.8%, which is in close competition with other types of semiconductor NCs.[44]

2. Results and Discussion

First, we demonstrate the synthesis of the seed NPLs needed for the final HI shell coating. The seed needs to lead to the best possible performance in terms of PLQY and low defect sites and to be thick enough so that they can endure the harsh reaction conditions at high temperatures, which is necessary for boosting up the thickness effectively for longer emission peak wavelengths. Starting with 4 ML CdSe core as the base material, all the forthcoming peripheral or vertical layers would be grown upon it. The core would be in a sandwich-like structure in which it is surrounded by crown and shells with different compositions and band alignments. **Figure 1**a depicts a schematic of all the steps with the main chemicals that are involved in formation of crown or shells. The size and alignment of the domains determine the wavefunctions of the electron and hole, which is critical for tuning the peak emission wavelength. Figure 1b demonstrates the bulk band alignment of CdSe, CdS, and ZnS, three compounds that participate in the formation of the final targeted heterostructure. The carrier wavefunctions leak into the shell, however, as it is centered around the core and all of the other layers have wider bandgaps, which energetically drives electron and hole pair to recombine through the lowest energy route, it is still expected that the final electron and hole recombination to occur in the core.

The absorption and emission spectra of CdSe core and CdSe/CdS core/crown are depicted in Figure S1a,b, Supporting Information, respectively, with their fluorescence decay curve presented in Figure S1c, Supporting Information. The first and second excitonic absorption peaks of the core are located at 510 and 479 nm corresponding to heavy and light hole transitions, respectively, with the emission peak is centered at 512 nm. A multiexponential decay function was fitted for each decay curve and the lifetime components were extracted from the best fit. CdSe/CdS core/crown NPLs exhibit an amplitude-averaged fluorescence lifetime (τ_{av}) of ≈3.6 ns, which is more than one order of magnitude longer than that of CdSe core. The multi-exponential decay behavior is an indicative of different channels with the fastest component usually attributed to the nonradiative decay pathway.[49] Addition of the CdS crown also causes a slight red-shift of the emission and absorption of CdSe core, which is due to the change in the dielectric constant and increase of the lateral size of the NPLs. The outermost layers of NPLs are passivated with a metal layer.[50] Incomplete passivation of the surface causes the charge carrier to be trapped and reduces emission, which decreases the PLQY.[31] For the CdSe/CdS core/crown NPLs, the peripheral surface of the core is effectively passivated with the crown, which in turn reduces the trapping and increases the PLQY. It is known that direct growth of shell layers on top of the core leads to reduced PLQY of the
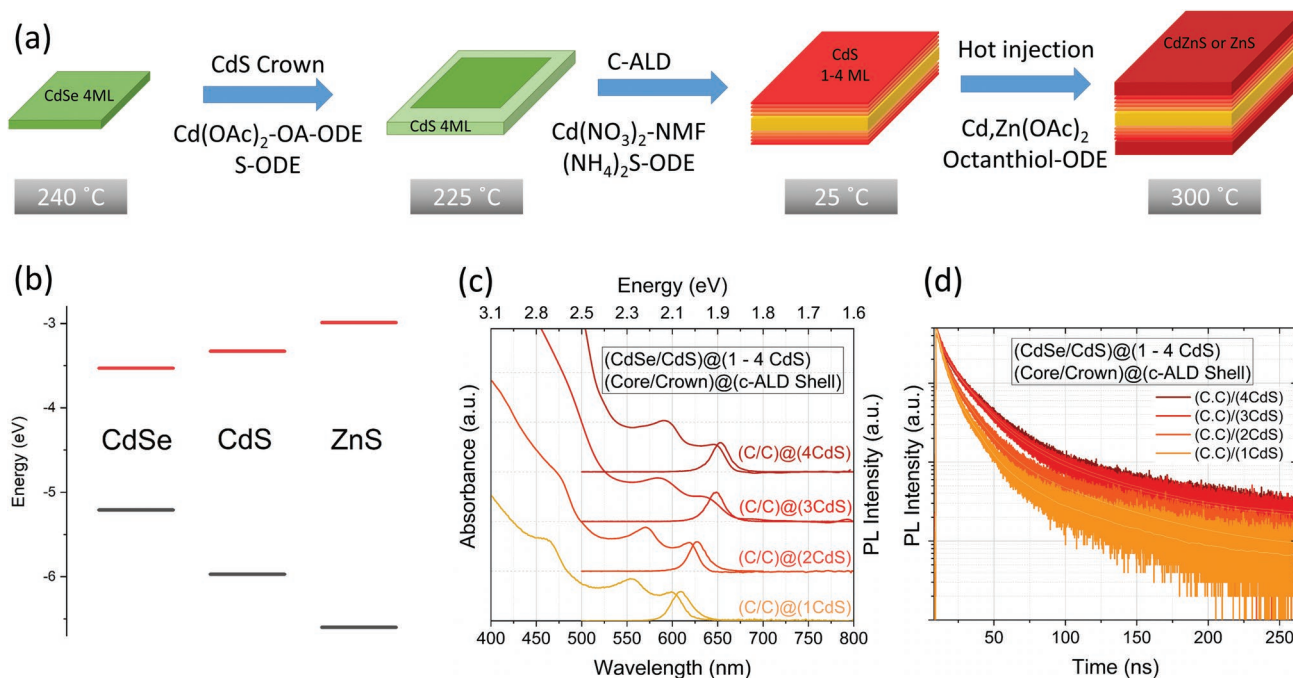
ADVANCED
SCIENCE NEWS
www.advancedsciencenews.com

NANO · MICRO
small
www.small-journal.com

Figure 1. a) A schematic of the synthesis pathway toward the final hetero-NPLs. First, bare CdSe core was laterally passivated with CdS crown, and then the c-ALD buffer layers were grown in the thickness direction to prepare the seeds. These seeds were used for the final HI shell coating. The thick NPLs were treated for longer times and using higher precursor concentrations during the hot injection. b) Band alignment of CdSe, CdS and ZnS. The numbers were extracted from refs. [55,56]. c) Absorbance and photoluminescence (PL) spectra, and d) TRF decay curves of (CdSe/CdS)@(1-4 CdS) (core/crown)@(c-ALD shell) seed NPLs.

NPLs, while the lateral passivation with a wider bandgap crown enhances PLQY.[27] For this reason, before c-ALD coating, the lateral sides of the CdSe core is passivated with a layer of CdS crown.[27,51] Deposition of a medium-sized crown leads to a threefold increase in the PLQY of the NPLs, which also manifests itself in longer recombination lifetime. Moreover, the growth of CdS crown increases the absorption cross-section of the NPLs at shorter wavelengths that act as an antenna for enhanced exciton formation, contributing to radiative recombination through exciton funneling into the core.[52,53]

It was shown previously that with the growth of CdS or ZnS HI shell on 4ML CdSe core reaching emission peak above 670 nm is not possible.[32,33] This in part is due to the lattice mismatch between different domains, which increases upon thickening of the shell. At the high growth temperature of 300 °C, the extra energy induced by lattice mismatch may be reduced, however the tendency for growth decreases. To overcome the thickness limitation, it is possible to include a buffer layer of CdS shell using c-ALD method, which has a much smaller lattice mismatch of 3.9%, compared to 12% for ZnS.[54] Moreover, the carriers wavefunction, especially of electron with a lower effective mass and a smaller band offset, relaxes into the CdS shell and causes a huge red-shift upon deposition of each layer. The red-shift in the case of (core/crown)@shell is larger than the core/shell, which is due to the change in dielectric constant.[27] The small band offset (Figure 1b) between the conduction band of CdSe and CdS also facilitates the electron wavefunction propagation leading to a quasi-Type-II structure. However, passivation of the outermost layers of NPLs with ZnS effectively increases the PLQY[33] owing to the enhancement of exciton confinement.

Herein, for the next step of the seed preparation, 1 to 4 monolayers of CdS shell were deposited on top of the core/crown NPLs with c-ALD method. This (core/crown)@(c-ALD shell) was later treated as the seed for hot injection, so that the thickness increases effectively and the core was passivated from all sides. Figure 1c,d shows the absorption and emission spectra and decay curves of (CdSe/CdS)@(1-4 CdS) (core/crown)@(c-ALD shell) NPLs, respectively. The absorption peak of CdS crown, which is originally located at 406 nm, red-shifts and disappears upon further c-ALD CdS shell growth, while the relaxation time increases from 3.6 ns for CdSe/CdS core/crown to 12.2 ns after deposition of 3 and 4 MLs of c-ALD CdS shell (Table S1, Supporting Information) owing to the higher spatial freedom of the excitons. The PLQY of the NPLs drops upon increasing the number of the c-ALD shells, which is due to poor passivation and defected structure of the NPL during the room temperature process. This also shows its effect in the same τ_{av} for 3 and 4 ML of CdS. However, the thickest NPLs exhibit a large red-shift to 652 nm in the emission peak with a FWHM of 22.1 nm.

In the next step, the (CdSe/CdS)@(1-4 CdS) (core/crown)@(c-ALD shell) NPLs were used as the seed for the upcoming hot injection shell growth, in order to increase the thickness. For the hot injection shell layer, two compositions of ZnS and CdZnS were chosen. As CdS has a narrower bandgap than ZnS, tuning the emission peak over longer wavelengths seems to be easier. However, CdS shell yields a lower PLQY than ZnS and would compromise the performance of the NPLs.[33] **Figure 2a,d** presents the absorption and emission spectra of (CdSe/CdS)@(1-4 CdS/ZnS) and (CdSe/CdS)@(1-4 CdS/CdZnS) (core/crown)@(c-ALD shell/HIS) heterostructures,
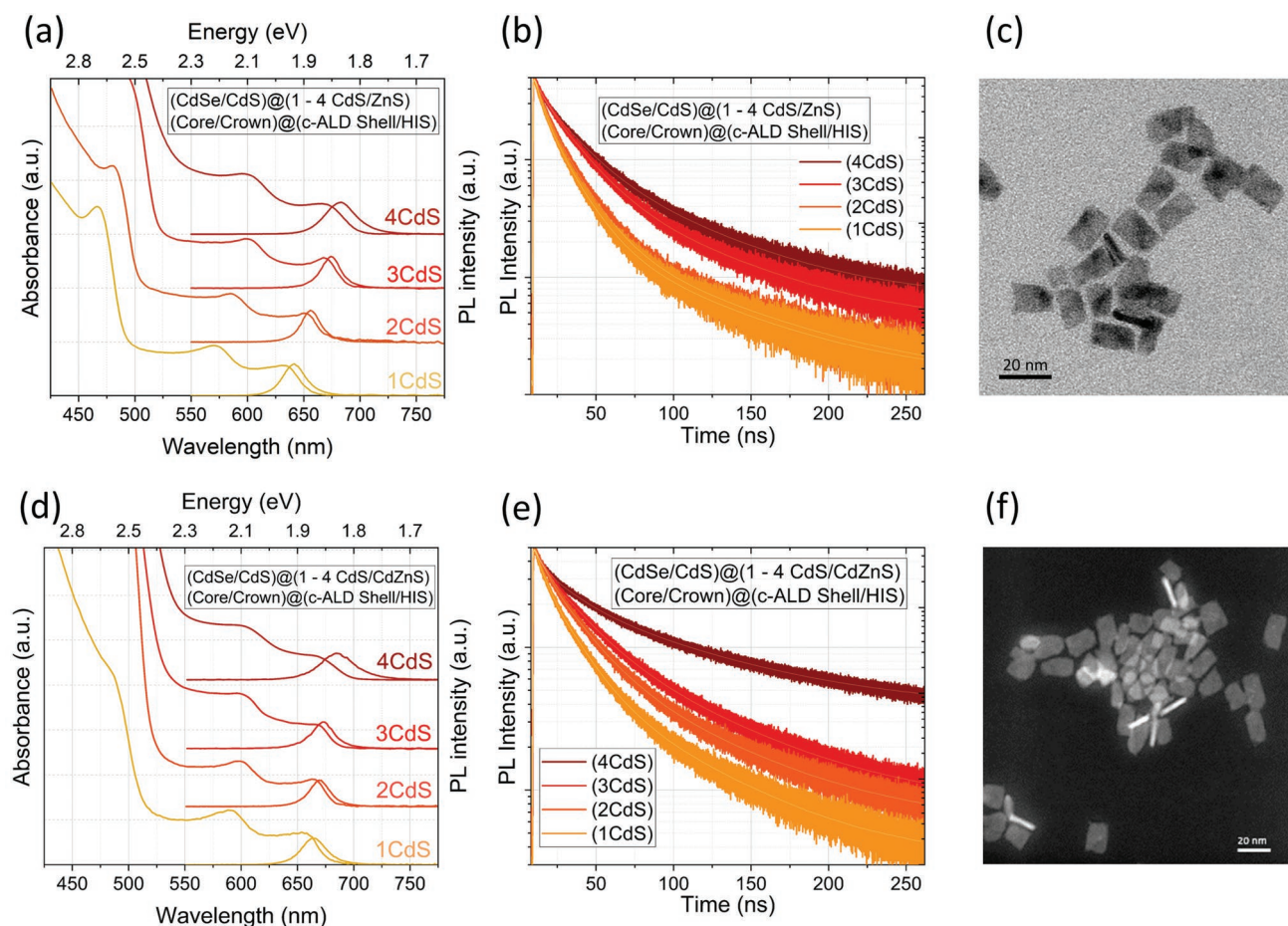
ADVANCED
SCIENCE NEWS

www.advancedsciencenews.com

NANO · MICRO

small

www.small-journal.com

Figure 2. a) Absorbance and photoluminescence spectra and b) TRF decay curves of HI shell NPLs with a generic heterostructure of (CdSe/CdS)@(1-4 CdS/ZnS) (core/crown)@(c-ALD/HI shell). c) TEM image of the NPLs with 4 ML of CdS buffer layers capped with ZnS HI shell showing a rectangular shape. d) Absorbance and PL spectra and e) TRF decay curves of HI shell NPLs with a generic heterostructure of (CdSe/CdS)@(1-4 CdS/CdZnS) (core/crown)@(c-ALD/HI shell). f) TEM image of NPLs with 4 ML of CdS buffer layers and final CdZnS HI shell. The shape of the NPLs is generally rectangular with less defined edges compared to the NPLs capped with ZnS HI shell. For both sets of samples, the growth time at 300 °C was between 1 and 2 h and the amount of Cd, Zn and injected S precursors were limited.

respectively. For all of the samples, the first and second excitonic peaks are in place, while their position is red-shifted compared to the initial seeds. This was predictable as the vertical growth of the shell would further loosen the tight confinement in the NPLs. The characteristic absorption peak of CdS crown also red-shifts toward higher wavelengths. This peak is obvious for the first two monolayers of c-ALD CdS shell when the HI shell is ZnS, but starts to fade away for CdZnS HIS even for 1 monolayer of CdS. The CdS crown peak is more prominently obvious for (CdSe/CdS)@(1-2 CdS/ZnS) NPLs than those of the (CdSe/CdS)@(1-2 CdS/CdZnS) NPLs, which is due to a sequence of events: During the hot injection shell growth, the outermost layers of the NPLs tend to etch in the initial stages,[40] which is mainly due to incomplete decomposition of $Cd(OAc)_2$ or $Zn(OAc)_2$ in the presence of oleylamine that accelerates the process.[55] Prior to the activation temperature of 1-octanthiol at around 260 °C, the extra dissolved Cd atoms with much higher chemical activity than Zn, will grow laterally on the seed NPLs, enlarging the lateral size and increasing its absorption in the blue region, at the cost of decreasing the thick-

ness. Moreover, at higher temperatures (>280 °C), Cd atoms can contribute to the shell formation faster than Zn atoms, hence making a thicker shell that covers the crown. While the peak absorbance ratio (A_{crown}/A_{core}) for CdSe/CdS core/crown and (CdSe/CdS)@(1CdS) (core/crown)@(c-ALD shell) is ≈1.7, the ratio significantly increases to 6 for (CdSe/CdS)@(1CdS/ZnS) (core/crown)@(c-ALD shell/HI shell) NPLs and drops to 5.5 for 2 ML of buffer layer. This observation further emphasizes the role of the CdS crown which, alongside with side passivation, can act as the protective layer that prevents etching of the core during the hot injection shell growth at the expense of its partial dissolution.

Tables S2 and S4, Supporting Information, list the emission peaks, FWHM and PLQY of the samples with CdZnS and ZnS HI shell, respectively. With larger conduction band offset energy of ZnS, the red-shift for ZnS HI shell is less prominent than the CdZnS HI shell. Moreover, the tendency for ZnS to grow is weaker than that of CdS, which means that under the same conditions (precursor concentration, growth time, etc.), a thinner shell of ZnS will be deposited, a problem that would be further

amplified by a higher lattice mismatch between CdSe core and ZnS shell in contrast to CdS shell. For the samples that are coated with ZnS, the emission wavelength covers a broad range from 641 to 679 nm while for CdZnS HI shell the emission peak is between 665 and 686 nm. The convergence of the emission peak wavelength for two different HI shells for the increasing number of CdS buffer layers implies that the growth rate of ZnS enhances as a result of the lower lattice mismatch. PLQY for ZnS HI shell remains above 80% (at a maximum of 97%) but it drops for CdZnS HI shell, which is an indicative of low cation diffusion at this growth time/temperature scale that maintains the outer shell layer for both set of NPLs. For ZnS HI shell NPLs, the outer shell layer is covered with ZnS that has a higher conduction band offset and prevents the electron wavefunction to reach the surface.

Figure 2b,e shows the decay curve of the samples. The average lifetimes (Tables S3 and S5, Supporting Information) of both samples increase with the shell thickness due to the expansion of electron-hole distance, with ZnS HI shell NPLs exhibiting lower τ_{av} than CdZnS HIS NPLs. This confirms the retention of ZnS outer layer with an increased spatial overlap of the carriers due to the large band offsets. The transmission electron microscope (TEM) images (Figure 2c,f) for NPLs with 4 ML CdS buffer layer show that they maintained their 2D shape, with one of the facets usually grown to a higher extend that prohibits the NPLs to have a perfect rectangular shape. CdZnS HI shell NPLs have a larger lateral size of $10.8 \pm 0.7 \times 19.7 \pm 0.7$ nm^2 with a thickness of 3.8 ± 0.3 nm than ZnS HIS NPLs of $9.9 \pm 0.8 \times 16.5 \pm 0.4$ nm^2 with a lower thickness of 2.8 ± 0.2 nm. The imperfect shape of NPLs is due to the limited growth time and the chemicals in the reaction that inhibits the shape focusing of the NPLs. For the thick shell samples, we will see that by providing enough time and reactants the shape evolves toward a more uniform rectangle.

The abovementioned heterostructure allows for the extension of emission peak to around 680 nm with acceptable properties. However, in order to reach a peak emission of 700 nm or above, extra addition of cation and anion precursors and extended growth time are required. In this regard, the same (core/crown)@(c-ALD Shell) seeds that were used before were prepared while the growth time was increased to 180–240 min, in comparison to 60–120 min for the previous samples. The recipe was also modified with the same composition of the hot injection shell, but the amount of the initial Zn and Cd precursors were doubled. Moreover, the anion precursor of 1-octanthiol was continued to be injected up until 10 mL (see the synthesis method in the Supporting Information for the details). The first effect of the altered recipe is modification of the shape of the NPLs, shown in **Figure 3**a,c. Compared to thin hot injection shell NPLs, the thick NPLs have much sharper edges with a well-defined square shape. The lateral size of the NPLs decreases along the longer dimension as a result of etching while it increases along the shorter one. For (CdSe/CdS)@(4CdS/CdZnS) (core/crown)@(c-ALD shell/(HI shell) NPLs, the lateral size is $13 \pm 1 \times 13 \pm 1$ nm^2 and the vertical thickness is 4.8 nm. Compared to thin shell NPLs, TEM images of thick shell NPLs show partial dissolution of the longer dimension that can recrystallize on the shorter sides, if enough time is given. Comparatively, the lateral size distribution increases for an ensemble of the NPLs, as the recrystallization also happens

in vertical direction, due to Ostwald ripening.[50] This suggests a dual shell growth mechanism, in which part of the cations and anions are provided from the precursor and the other part is the result of opening windows during each cycle of Ostwald ripening, as was discussed elsewhere.[50] Figure 3b shows a TEM side image of the thick NPLs, with an obvious contrast between the core and the shell. The CdSe core and CdS crown contain heavy element of Cd which has a higher contrast than ZnS such that, even with partial disintegration of periphery of the NPLs, the core remains intact in its place.

Figure 3d shows the absorption and emission spectra of (core/crown)@(c-ALD shell/thick HIS) for samples that have 3 or 4 monolayers of CdS c-ALD shell, and thick HIS of either ZnS or CdZnS. While reaching longer wavelength emissions is not feasible with hot injection shell growth on mere CdSe core, it is possible to go beyond 700 nm emission peak, closer to the theoretical bulk bandgap of CdSe, if the hot injection is performed on (core/crown)@(c-ALD shell) seeds. As the shell grows bigger, the emission bandwidth broadens and PLQY decreases. The loosened exciton confinement due to the increased thickness is partially responsible for this broadening. However, due to Ostwald ripening, the lateral/thickness size distribution may increase and result in small inhomogeneous broadening. Also, as the thickness increases the probability of formation of defects with surface or strain nature is increasing, which suppresses the PLQY. Figure S2, Supporting Information, shows the absorption and emission spectra of a test sample with 2 ML of intermediate c-ALD shell. The sample was treated with the same thick HI shell growth process, however the growth time was substantially increased to 360 min so that an emission peak near 700 nm becomes achievable. The emission spectrum is extremely broadened with a FWHM of 52 nm, and the PLQY also drops below 2%. This is a further emphasis on the role of the intermediate c-ALD shell, which would alleviate the lattice mismatch strain between different domains. The long shell growth time at high temperature also facilitates the diffusion and reorganization of the cations, as was previously shown.[40] During this time, the distribution of Zn and Cd changes and makes a gradient alloyed structure in the shell, where the strain is reduced and the outermost layer is composed of mostly ZnS.

Figure 3e shows the decay curve of the thick NPLs (for which the decay components are listed in Table S7, Supporting Information). Two sets of NPLs that are coated with final CdZnS HIS have a slower decay rate than the ZnS coated NPLs, in accordance with their longer emission wavelength and thickness. For thick ZnS HIS NPLs, the average lifetime does not show a significant change in spite of their thicker shell, which confirms the diffusion and reorganization of Zn to outer layers. Moreover, the pure ZnS shell is more susceptible to generating defect sites because of its lower affinity to bind to the surface, which also reflects its effect on lower QY. The best optimized sample that emits at 701 nm is (core/crown)@(4CdS/CdZnS) NPLs with a PLQY of 88% and a FWHM of 26 nm. Its average lifetime is higher than thin NPLs of the same class but yet almost equal to NPLs with 3 ML of buffer layer. In this sample, the interplay among the shell growth, surface passivation and cation reorganization preserves the properties and thickness. The multi-exponential decay behavior of this sample mainly originates from
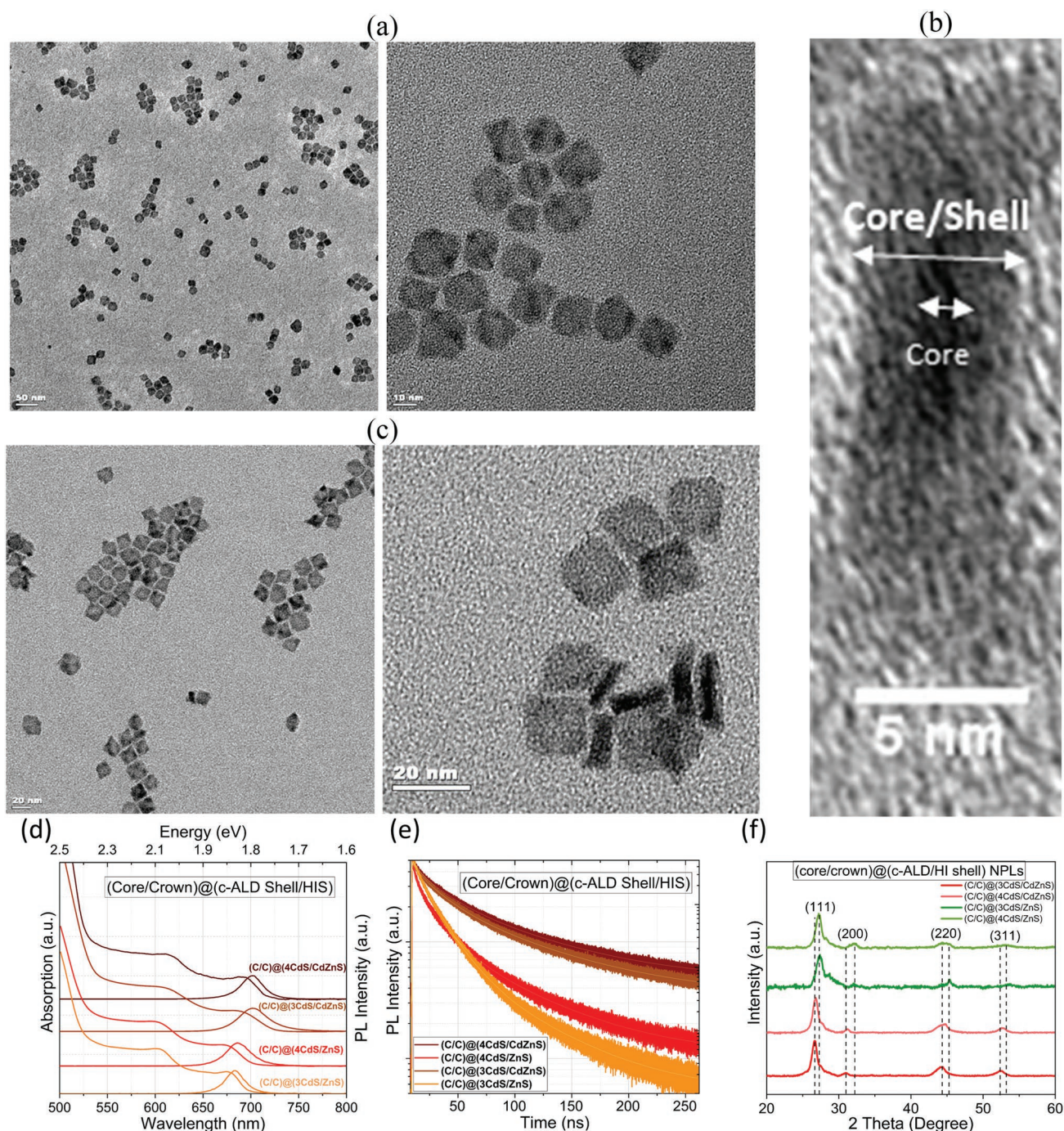
Figure 3. TEM images of thick NPLs that were treated with higher concentrations of the precursors for a prolonged time: a) NPLs with 3 ML of CdS buffer layer, with a heterostructure of (CdSe/CdS)@(3CdS/CdZnS) (core/crown)@(c-ALD shell/(HI shell), b,c) NPLs with 4 ML of CdS buffer layer, with a heterostructure of (CdSe/CdS)@(4CdS/CdZnS) (core/crown)@(c-ALD shell/(HI shell). For both of the samples the shape has become more symmetric compared to the previous rectangular NPLs. d) Absorbance and PL spectra, e) TRF decay curves, and f) X-ray diffraction patterns of thick (core/crown)@(c-ALD/HI shell) NPLs. All of the samples were treated between 3 and 4 h for the shell growth at 300 °C and the amount of Cd and Zn precursors were doubled in comparison to thin shell NPLs.

a possible nonradiative channel, with usually the fastest decay rate. It was previously shown that even for core/shell NPLs possessing near-unity PLQY (close to but less than 100%) it has not been possible to reach a mono-exponential decay, however for these samples the share of the fast decay channel would be very low.[33] In our best sample, less than 1% of the recombination share is coming from the fastest channel (4.4 ns) which has a value in the order of previously reported nonradiative channel of core/shell NPLs.[56] The rest 99% of the emission contribution is coming from the two longest components (78.3 and

19.8 ns) (Table S7, Supporting Information), which have far higher characteristic lifetime rates than the usual nonradiative channels. This indicates reasonably high surface passivation, suppressing otherwise strong nonradiative channels possibly originating from the surface traps to a good extent.

The X-ray diffraction pattern in Figure 3f shows that the diffraction peak position of the NPLs match with bulk CdS and ZnS, with a slight increase in the diffracted angle when the ZnS shell is coated, which is due to shell alloying. Since all of the domains have the same crystalline structure of zinc blende and all the NPLs consist of a dominantly thick shell, all of the NPLs have a similar diffraction pattern with a slight shift of the peaks. ZnS has the smallest lattice constant compared to CdSe and CdS, hence the ZnS HIS NPLs show a small emergence of ZnS peak at $\approx 2\theta$ of 29°, near to the bulk peak of ZnS for stronger plane of (111), because of their higher probability of pure and thicker ZnS shell formation. X-ray photoelectron spectroscopy (XPS) presented in Figure S3, Supporting Information, provides information about the binding energy of cadmium, zinc, selenium, and sulfur and their chemical states. No other species is formed through thick shelling, or otherwise they were successfully filtered out through standard cleaning procedure. Neither Se nor S is oxidized after the synthesis, as may be the case for the chalcogenides.

As discussed above, the synthesized CdSe-based NPLs present a high PLQY and a narrow FWHM in the deep-red spectral region. In the final section, CQW-LEDs based on these NPLs were prepared to confirm their outstanding electroluminescence properties. The CQW-LEDs were fabricated using our deep-red NPLs in the device configuration of indium tin oxide (ITO)/poly(3,4-ethylenedioxythiophene) polystyrene sulfonate (PEDOT:PSS)/Poly(N,N''-bis-4-butylphenyl-N,N''-bisphenyl) benzidine (poly-TPD)/Poly(9-vinylcarbazole) (PVK)/NPLs/zinc oxide (ZnO)/Al (**Figure 4**a). In Figure 4a, the energy levels for ZnO were extracted from the literature[57] and for the CQWs were calculate directly from the XPS measurement based on a published method (the details of which is given in the Supporting Information).[58] Figure 4b shows the cross-sectional image of the resulting LED device. Due to poor contrast between ZnO and thick NPLs layer, they cannot be distinguished from each other. In this device structure, ITO is employed as the anode, PEDOT:PSS as the hole injection layer (HIL), poly-TPD, PVK as the co-hole transport layer (co-HTL), NPLs as the emitting layer (EML), ZnO as the electron transport layer (ETL), and Al as the cathode contact. The co-HTL, consisting of poly-TPD/ PVK, is designed to benefit from both the high hole mobility provided by poly-TPD (1×10^{-4} cm^2 V^{-1} s^{-1}), and deep highest-occupied-molecular-orbit energy level (−5.8 eV) provided by PVK.[59] Using this architecture, the stepwise energy level alignment between ITO and HIL/HTL ensures an efficient hole injection into the EML (Figure 4a). In an all-in-solution LED structure, ZnO nanocrystals are commonly used as ETL. It is
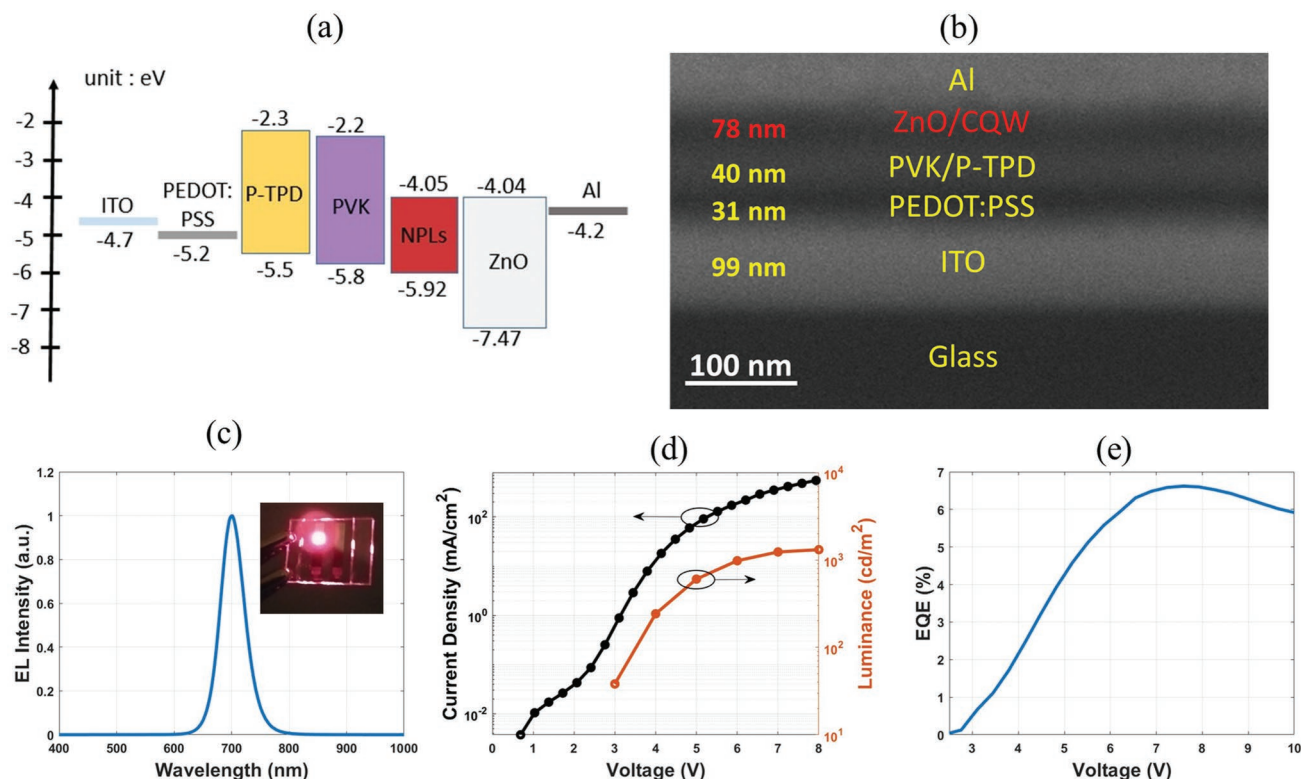

Figure 4. a) LED device structure and flat band energy level diagram. The values for NPLs energy levels were measured directly from the XPS measurement according to the method used previously.[58] The energy levels for ZnO were extracted from the literature[57] and those of other layers were taken from the catalogs of their materials. b) Cross-sectional scanning electron microscopy image of the device showing the layers with different contrasts. c) Electroluminescence spectrum at an applied bias of 8 V, d) current density and luminance versus voltage, and e) EQE versus driving voltage, all for the deep-red emitting CQW-LED with (core/crown)@(4CdS/CdZnS) NPLs as the active material.

synthesized via easy in-solution process at ambient temperature and without the need of any specific condition. Their relatively high electron mobility and proper energy level allow efficient electron injection into the EML.[60,61] However, when only poly-TPD or PVK is used as the HTL, the hole injection would not be as high as that of the electrons through ZnO layer, which may cause charge imbalance in the EML lead to increased non-radiative Auger recombination.[62] To address this problem, we used poly-TPD/PVK as the stepwise co-HTLs, which allows for a better charge balance.

Figure 4c presents the normalized electroluminescence of the deep-red CQW-LED with one symmetric peak centered around 701 nm, which is the deepest red CQW-LED reported in the literature to our knowledge. The device performance of the CQW-LED are shown in Figure 4d,e. The turn-on voltage (V_{on}) of our CQW-LED is ≈2.4 V and the maximum power efficiency of it is 21.3 lm W^{-1}. The current density–voltage (black) and luminance–voltage (orange) graphs show steady increase with a maximum brightness level of 1300 cd m^{-2} at the operating voltage of 8 V, and the maximum EQE of 6.8% was achieved at the applied voltage of 7.5 V. Another CQW-LED devices that was fabricated from the heterostructure of (core/crown)@(4CdS/ZnS) exhibits an EL peak centered around 689 nm with an EQE of 5.3% (Figure S4, Supporting Information). The results are a clear proof of capability of these NPLs as the active material for longer wavelength electroluminescent LEDs.

As discussed before, the NPLs reported to date emit in the visible range of the light; hence no report of the electroluminescence properties of NPLs at longer wavelengths can be found. However, the peak EQE of our device surpasses many of the best reported nanomaterials emitting in the vicinity of 660–740 nm.[44,63] Table S8, Supporting Information, lists the performance of other types of LEDs with different active materials of mainly perovskites. Considering our previous report on CdSe-based CQW-LEDs,[35] our device in this current work demonstrates widely extended spectral tunability into the deep-red region, along with an excellent EQE, which outcompetes the perovskite-LEDs in terms of the performance in this spectral range.

3. Conclusion

In conclusion, a systematic pathway was designed to increase the thickness of NPLs and push the emission peak wavelength to extend the range of tunability while maintaining the excellent properties of the NPLs. Unlike the conventional HI method where CdSe core is used directly as the seed, here we first synthesized thick NPLs seeds that contain a passivating medium-size CdS crown, and then through consecutive c-ALD cycles, CdS shell was grown on top of them. This strategy is proved to be effective for the growth of final HI shell, as it can overcome the barrier that may hinder the deposition of extra shell layers with a minimum increase of the defect density and incoherent shell growth. The interplay between the lower bandgap CdS and the surface passivation of ZnS make it possible to find the best tradeoff between the tunability and properties. It was shown that by alloying the HI shell from ZnS to CdZnS it is possible to reach longer wavelengths while reducing the

surface passivation effect through the high bandgap ZnS. Our best performance NPLs emits at 701 nm with QY of 88% and FWHM of 26 nm. At the end, the LED device with mentioned structure was fabricated with the thick NPLs as the active material, which exhibits the highest EQE of 6.8% at the emission wavelength of 701 nm. These results should encourage further investigation of such advanced heterostructures of NPLs into the deep-red to near-infrared high-performance LEDs based on II–VI semiconductors, which can possibly compete with other types of semiconductor LEDs.

Supporting Information

Acknowledgements

Conflict of Interest

The authors declare no conflict of interest.

Data Availability Statement

The data that support the findings of this study are available in the supplementary material of this article.

Keywords

[1] S. Ithurria, G. Bousquet, B. Dubertret, *J. Am. Chem. Soc.* **2011**, *133*, 3070.

[2] M. Nasilowski, B. Mahler, E. Lhuillier, S. Ithurria, B. Dubertret, *Chem. Rev.* **2016**, *116*, 10934.

[3] E. V. Shornikova, L. Biadala, D. R. Yakovlev, V. F. Sapega, Y. G. Kusrayev, A. A. Mitioglu, M. V. Ballottin, P. C. M. Christianen, V. V. Belykh, M. V. Kochiev, N. N. Sibeldin, A. A. Golovatenko, A. V. Rodina, N. A. Gippius, A. Kuntzmann, Y. Jiang, M. Nasilowski, B. Dubertret, M. Bayer, *Nanoscale* **2018**, *10*, 646.

[4] Y. Min, E. Im, G.-T. Hwang, J.-W. Kim, C.-W. Ahn, J.-J. Choi, B.-D. Hahn, J.-H. Choi, W.-H. Yoon, D.-S. Park, D. C. Hyun, G. D. Moon, *Nano Res.* **2019**, *12*, 1750.

[5] S. Delikanli, G. Yu, A. Yeltik, S. Bose, T. Erdem, J. Yu, O. Erdem, M. Sharma, V. K. Sharma, U. Quliyeva, S. Shendre, C. Dang,

ADVANCED
SCIENCE NEWS
www.advancedsciencenews.com

NANO · MICRO
small
www.small-journal.com

D. H. Zhang, T. C. Sum, W. Fan, H. V. Demir, *Adv. Funct. Mater.* **2019**, *29*, 1901028.

[6] J. C. Van Der Bok, D. M. Dekker, M. L. J. Peerlings, B. B. V. Salzmann, A. Meijerink, *J. Phys. Chem. C* **2020**, *124*, 12153.

[7] M. Sharma, K. Gungor, A. Yeltik, M. Olutas, B. Guzelturk, Y. Kelestemur, T. Erdem, S. Delikanli, J. R. McBride, H. V. Demir, *Adv. Mater.* **2017**, *29*, 1700821.

[8] E. Lhuillier, J. F. Dayen, D. O. Thomas, A. Robin, B. Doudin, B. Dubertret, *Nano Lett.* **2015**, *15*, 1736.

[9] N. Gheshlaghi, S. Foroutan-Barenji, O. Erdem, Y. Altintas, F. Shabani, M. H. Humayun, H. V. Demir, *Nano Lett.* **2021**, *21*, 4598.

[10] S. Delikanli, O. Erdem, F. Isik, H. D. Baruj, F. Shabani, H. B. Yagci, E. G. Durmusoglu, H. V. Demir, *J. Phys. Chem. Lett.* **2021**, *12*, 2177.

[11] S. Foroutan-Barenji, O. Erdem, N. Gheshlaghi, Y. Altintas, H. V. Demir, *Small* **2020**, *16*, 2004304.

[12] E. Ebrahimi, M. Irfan, F. Shabani, Y. Kocak, B. Karakurt, E. Erdem, H. V. Demir, E. Ozensoy, *ChemCatChem* **2020**, *12*, 6329.

[13] A. W. Achtstein, R. Scott, S. Kickhöfel, S. T. Jagsch, S. Christodoulou, G. H. V. Bertrand, A. V. Prudnikau, A. Antanovich, M. Artemyev, I. Moreels, A. Schliwa, U. Woggon, *Phys. Rev. Lett.* **2016**, *116*, 116802.

[14] R. Benchamekh, N. A. Gippius, J. Even, M. O. Nestoklon, J. M. Jancu, S. Ithurria, B. Dubertret, A. L. Efros, P. Voisin, *Phys. Rev. B: Condens. Matter Mater. Phys.* **2014**, *89*, 035307.

[15] Q. Li, T. Lian, *Chem. Sci.* **2018**, *9*, 728.

[16] A. W. Achtstein, A. Antanovich, A. Prudnikau, R. Scott, U. Woggon, M. Artemyev, *J. Phys. Chem. C* **2015**, *119*, 20156.

[17] M. H. Humayun, P. L. Hernandez-Martinez, N. Gheshlaghi, O. Erdem, Y. Altintas, F. Shabani, H. V. Demir, *Small* **2021**, *17*, 2103524.

[18] A. Yeltik, S. Delikanli, M. Olutas, Y. Kelestemur, B. Guzelturk, H. V. Demir, *J. Phys. Chem. C* **2015**, *119*, 26768.

[19] M. D. Tessier, C. Javaux, I. Maksimovic, V. Loriette, B. Dubertret, *ACS Nano* **2012**, *6*, 6751.

[20] C. She, I. Fedin, D. S. Dolzhnikov, P. D. Dahlberg, G. S. Engel, R. D. Schaller, D. V. Talapin, *ACS Nano* **2015**, *9*, 9475.

[21] A. Riedinger, F. D. Ott, A. Mule, S. Mazzotti, P. N. Knüsel, S. J. P. Kress, F. Prins, S. C. Erwin, D. J. Norris, *Nat. Mater.* **2017**, *16*, 743.

[22] N. Moghaddam, C. Dabard, M. Dufour, H. Po, X. Xu, T. Pons, E. Lhuillier, S. Ithurria, *J. Am. Chem. Soc.* **2021**, *143*, 1863.

[23] W. Cho, S. Kim, I. Coropceanu, V. Srivastava, B. T. Diroll, A. Hazarika, I. Fedin, G. Galli, R. D. Schaller, D. V. Talapin, *Chem. Mater.* **2018**, *30*, 6957.

[24] S. Christodoulou, J. I. Climente, J. Planelles, R. Brescia, M. Prato, B. Martín-Garciá, A. H. Khan, I. Moreels, *Nano Lett.* **2018**, *18*, 6248.

[25] A. Chu, C. Livache, S. Ithurria, E. Lhuillier, *J. Appl. Phys.* **2018**, *123*, 035701.

[26] A. Hazarika, I. Fedin, L. Hong, J. Guo, V. Srivastava, W. Cho, I. Coropceanu, J. Portner, B. T. Diroll, J. P. Philbin, E. Rabani, R. Klie, D. V. Talapin, *J. Am. Chem. Soc.* **2019**, *141*, 13487.

[27] Y. Kelestemur, B. Guzelturk, O. Erdem, M. Olutas, K. Gungor, H. V. Demir, *Adv. Funct. Mater.* **2016**, *26*, 3570.

[28] A. Polovitsyn, Z. Dang, J. L. Movilla, B. Martín-García, A. H. Khan, G. H. V. Bertrand, R. Brescia, I. Moreels, *Chem. Mater.* **2017**, *29*, 5671.

[29] C. Meerbach, R. Tietze, S. Voigt, V. Sayevich, V. M. Dzhagan, S. C. Erwin, Z. Dang, O. Selyshchev, K. Schneider, D. R. T. Zahn, V. Lesnyak, A. Eychmüller, *Adv. Opt. Mater.* **2019**, *7*, 1801478.

[30] M. D. Tessier, P. Spinicelli, D. Dupont, G. Patriarche, S. Ithurria, B. Dubertret, *Nano Lett.* **2014**, *14*, 207.

[31] M. D. Tessier, B. Mahler, B. Nadal, H. Heuclin, S. Pedetti, B. Dubertret, *Nano Lett.* **2013**, *13*, 3321.

[32] A. A. Rossinelli, A. Riedinger, P. Marqués-Gallego, P. N. Knüsel, F. V. Antolinez, D. J. Norris, *Chem. Commun.* **2017**, *53*, 9938.

[33] Y. Altintas, U. Quliyeva, K. Gungor, O. Erdem, Y. Kelestemur, E. Mutlugun, M. V. Kovalenko, H. V. Demir, *Small* **2019**, *15*, 1804854.

[34] Y. Altintas, K. Gungor, Y. Gao, M. Sak, U. Quliyeva, G. Bappi, E. Mutlugun, E. H. Sargent, H. V. Demir, *ACS Nano* **2019**, *13*, 10662.

[35] Y. Altintas, B. Liu, P. L. Hernández-Martínez, N. Gheshlaghi, F. Shabani, M. Sharma, L. Wang, H. Sun, E. Mutlugun, H. V. Demir, *Chem. Mater.* **2020**, *32*, 7874.

[36] L. Zhao, L. Hu, X. Fang, *Adv. Funct. Mater.* **2012**, *22*, 1551.

[37] Y. Chen, J. Vela, H. Htoon, J. L. Casson, D. J. Werder, D. A. Bussian, V. I. Klimov, J. A. Hollingsworth, *J. Am. Chem. Soc.* **2008**, *130*, 5026.

[38] C. Galland, S. Brovelli, W. K. Bae, L. A. Padilha, F. Meinardi, V. I. Klimov, *Nano Lett.* **2013**, *13*, 321.

[39] S. Brovelli, W. K. Bae, C. Galland, U. Giovanella, F. Meinardi, V. I. Klimov, *Nano Lett.* **2014**, *14*, 486.

[40] A. A. Rossinelli, H. Rojo, A. S. Mule, M. Aellen, A. Cocina, E. De Leo, R. Schäublin, D. J. Norris, *Chem. Mater.* **2019**, *31*, 9567.

[41] Y. Kelestemur, Y. Shynkarenko, M. Anni, S. Yakunin, M. L. De Giorgi, M. V. Kovalenko, *ACS Nano* **2019**, *13*, 13899.

[42] J. Zhang, Y. Sun, S. Ye, J. Song, J. Qu, *Chem. Mater.* **2020**, *32*, 9490.

[43] H. Lu, G. M. Carroll, N. R. Neale, M. C. Beard, *ACS Nano* **2019**, *13*, 939.

[44] P. Vashishtha, S. Bishnoi, C. H. A. Li, M. Jagadeeswararao, T. J. N. Hooper, N. Lohia, S. B. Shivarudraiah, M. S. Ansari, S. N. Sharma, J. E. Halpert, *ACS Appl. Electron. Mater.* **2020**, *2*, 3470.

[45] B. Liu, Y. Altintas, L. Wang, S. Shendre, M. Sharma, H. Sun, E. Mutlugun, H. V. Demir, *Adv. Mater.* **2020**, *32*, 1905824.

[46] Y. Zheng, X. Zhu, *Org. Mater.* **2020**, *2*, 253.

[47] D. Hertel, H. Maréchal, D. A. Tefera, W. Fan, R. Hicks, *A Low-Cost VIS-NIR True Color Night Vision Video System Based on a Wide Dynamic Range CMOS Imager*, In 2009 IEEE Intelligent Vehicles Symposium, IEEE **2009**, pp. 273–278.

[48] A. M. Smith, M. C. Mancini, S. Nie, *Nat. Nanotechnol.* **2009**, *4*, 710.

[49] L. Biadala, F. Liu, M. D. Tessier, D. R. Yakovlev, B. Dubertret, M. Bayer, *Nano Lett.* **2014**, *14*, 1134.

[50] F. D. Ott, A. Riedinger, D. R. Ochsenbein, P. N. Knüsel, S. C. Erwin, M. Mazzotti, D. J. Norris, *Nano Lett.* **2017**, *17*, 6870.

[51] S. Shendre, S. Delikanli, M. Li, D. Dede, Z. Pan, S. T. Ha, Y. H. Fu, P. L. Hernández-Martínez, J. Yu, O. Erdem, A. I. Kuznetsov, C. Dang, T. C. Sum, H. V. Demir, *Nanoscale* **2019**, *11*, 301.

[52] D. V. Talapin, J. H. Nelson, E. V. Shevchenko, S. Aloni, B. Sadtler, A. P. Alivisatos, *Nano Lett.* **2007**, *7*, 2951.

[53] N. J. Borys, M. J. Walter, J. Huang, D. V. Talapin, J. M. Lupton, *Science* **2010**, *330*, 1371.

[54] R. Xie, U. Kolb, J. Li, T. Basché, A. Mews, *J. Am. Chem. Soc.* **2005**, *127*, 7480.

[55] I. Fedin, D. V. Talapin, *J. Am. Chem. Soc.* **2016**, *138*, 9771.

[56] L. T. Kunneman, J. M. Schins, S. Pedetti, H. Heuclin, F. C. Grozema, A. J. Houtepen, B. Dubertret, L. D. A. Siebbeles, *Nano Lett.* **2014**, *14*, 7039.

[57] B. Liu, M. Sharma, J. Yu, S. Shendre, C. Hettiarachchi, A. Sharma, A. Yeltik, L. Wang, H. Sun, C. Dang, H. V. Demir, B. Liu, M. Sharma, J. Yu, S. Shendre, A. Sharma, C. Dang, H. V. Demir, C. Hettiarachchi, A. Yeltik, L. Wang, H. Sun, *Small* **2019**, *15*, 1901983.

[58] E. M. Miller, D. M. Kroupa, J. Zhang, P. Schulz, A. R. Marshall, A. Kahn, S. Lany, J. M. Luther, M. C. Beard, C. L. Perkins, J. Van De Lagemaat, *ACS Nano* **2016**, *10*, 3302.

[59] X. Dai, Z. Zhang, Y. Jin, Y. Niu, H. Cao, X. Liang, L. Chen, J. Wang, X. Peng, *Nature* **2014**, *515*, 96.

[60] H. Y. Kim, Y. J. Park, J. Kim, C. J. Han, J. Lee, Y. Kim, T. Greco, C. Ippen, A. Wedel, B. K. Ju, M. S. Oh, *Adv. Funct. Mater.* **2016**, *26*, 3454.

[61] L. Qian, Y. Zheng, J. Xue, P. H. Holloway, *Nat. Photonics* **2011**, *5*, 543.

[62] Q. Zeng, Z. Xu, C. Zheng, Y. Liu, W. Chen, T. Guo, F. Li, C. Xiang, Y. Yang, W. Cao, X. Xie, X. Yan, L. Qian, P. H. Holloway, *ACS Appl. Mater. Interfaces* **2018**, *10*, 8258.

[63] I. Lignos, V. Morad, Y. Shynkarenko, C. Bernasconi, R. M. Maceiczyk, L. Protesescu, F. Bertolotti, S. Kumar, S. T. Ochsenbein, N. Masciocchi, A. Guagliardi, C. J. Shih, M. I. Bodnarchuk, A. J. Demello, M. V. Kovalenko, *ACS Nano* **2018**, *12*, 5504.